Waveform inversion of *SS* precursors: An investigation of the northwestern Pacific subduction zones and intraplate volcanoes in China

Ramin M.H. Dokht *, Yu Jeffrey Gu, Mauricio D. Sacchi

Department of Physics, University of Alberta, Edmonton, AB T6G2E1, Canada

ABSTRACT

The arrival time and amplitude of underside reflections from mantle seismic discontinuities (*SS* precursors) have made major contributions to the understanding of mantle composition and dynamics. In this study, we introduce a nonlinear waveform inversion technique to simultaneously constrain shear velocities and discontinuity depths beneath the northwestern Pacific subduction system. Based exclusively on a large *SS* precursor waveform dataset, we are able to clearly delineate the morphology of the descending Pacific plate, which flattens at the base of the upper mantle and extends westward by ~1500 km toward northern-central China. Our grid search yields the maximum correlation between shear velocity and transition zone thickness at an angle of ~30°, consistent with the reported average slab dip beneath the study region. The strongly positive correlation suggests predominantly thermal, rather than compositional, variations along the descending Pacific plate. The joint depth-velocity solution also shows a 5–10 km depression of the 410 km discontinuity and an average decrease of 1.2% in upper mantle shear velocity beneath the intraplate volcanic fields in northeastern China. This anomaly, which reaches the middle of the upper mantle transition zone beneath the Changbai hotspot, initiates at a significantly shallower (~320 km) depth beneath the Wudalianchi region. High amplitude reflections at depths greater than 410 km suggest a water-poor melt layer in possible association with 1) decompression melting from passive upwelling and/or 2) active upwelling through a slab window.

© 2016 International Association for Gondwana Research. Published by Elsevier B.V. All rights reserved.

1. Introduction

Intraplate volcanic activities have been well documented in both continental and oceanic regions at distances of hundreds to thousands of kilometers away from plate boundary zones. The origin and mechanism of intraplate volcanism vary broadly (Niu, 2005; Zhao, 2007; Tang et al., 2014) and often require the presence of deep mantle plumes (Campbell, 2007; Chen et al., 2007; Zhao, 2007). An ideal laboratory for the study of intraplate volcanism is northeastern (NE) Asia, where Cenozoic magmatic centers are densely distributed along the north-south oriented Changbai Mountain range and Wudalianchi volcanic field in NE China. The former is a stratovolcano located approximately 1200 km west of the Japan trench, while the latter consists of cinder volcanoes covering an area of 500 km^2 toward the north. The origin of these volcanic fields has been linked to mantle plumes as well as subduction-related back-arc spreading and thinning of the lithosphere (Basu et al., 1991; Niu, 2005), though compatible helium isotopic compositions between the Cenozoic basalts from the same region and mid-ocean ridge basalt favor an upper mantle origin (Chen et al.,

2007). Further insights were provided by seismic tomography where a horizontally deflected and stagnant Pacific plate at the base of the upper mantle could play a key role in melt generation (Gorbatov and Kennett, 2003; Zhao et al., 2004; Obayashi et al., 2006; Lebedev and van der Hilst, 2008; Li and van der Hilst, 2010).

Models of seismic velocities are complemented by observations of mantle transition zone (MTZ) discontinuities. For the upper mantle assemblage of olivine composition, phase transitions from olivine to wadsleyite and ringwoodite dissociation are widely accepted origins of the 410 km discontinuity (from here on, 410) and 660 km discontinuity (from here on, 660), respectively, at the top and bottom of the MTZ (Anderson, 1967; Ito and Takahashi, 1989). These two mineralogical phase boundaries exhibit opposite Clapeyron slopes (Navrotsky, 1980; Ito and Takahashi, 1989; Katsura and Ito, 1989; Weidner and Wang, 1998), and their sensitivities to temperature and composition have been frequently explored in mantle seismic imaging (Shearer, 1993; Gu et al., 1998; Gu and Dziewonski, 2002; Lawrence and Shearer, 2006a; Deuss, 2009). Based on mantle reflections (Heit et al., 2010; Gu et al., 2012) and conversions (Li and Yuan, 2003; Liu et al., 2015), a depression in excess of 30 km has been observed at the base of the MTZ beneath the intraplate volcanic fields in NE China. This topographic anomaly coincides with a distinctive low velocity asthenosphere, which has been interpreted as the potential source of melting beneath

* Corresponding author.
E-mail address: ramin1@ualberta.ca (R.M.H. Dokht).

the volcanic centers (Zhao et al., 2004; Lei and Zhao, 2005; Niu, 2005; Li and van der Hilst, 2010; Tang et al., 2014).

A known source of error in the independent analyses of seismic velocity and discontinuity topography is the trade-off between them (Flanagan and Shearer, 1998; Gu and Dziewonski, 2002; Zhao et al., 2004; Obayashi et al., 2006; Li et al., 2008; Li and van der Hilst, 2010). Time corrections are typically adopted to minimize the excess topography caused by heterogeneous mantle structures, whereas models of seismic velocities are mostly derived under the assumption of unperturbed mantle interfacial depths. This trade-off was reduced by Gu et al. (2003) and Lawrence and Shearer (2006a) through joint inversions of seismic velocity and discontinuity topography, though much of the information embedded in the waveforms of the secondary reflections was underutilized. In this study we characterize the upper mantle and MTZ beneath the northwestern Pacific region (Fig. 1) using waveform inversions of stacked *SS* precursors (Fig. 1d). Our full waveform nonlinear inversion approach recovers a simultaneous solution for the travel times of *SS* precursors, which are sensitive to mantle temperatures surrounding olivine phase boundaries (Ohtani et al., 2004; Deuss, 2009; Lessing et al., 2014), and the impedance contrasts imprinted onto the *SS* precursor amplitudes (Shearer, 1991; Chambers et al., 2005; Gu and Sacchi, 2009; Lessing et al., 2015). We will demonstrate that a dense precursor dataset alone is sufficient to resolve major

upper mantle seismic anomalies in the northwestern Pacific subduction system.

2. Data and method

We utilize a global dataset of broadband and long-period seismograms, recorded between 2006 and 2014, from the Incorporated Research Institutions for Seismology (IRIS). The midpoints of the source-receiver pairs densely sample the structure beneath NE China and the northwestern Pacific subduction zones. We restricted the maximum depth of earthquakes to 75 km to mitigate the interference of depth phases (Schmerr and Garnero, 2006; An et al., 2007) and adopt a minimum magnitude (Mw) cutoff of 5.5 to ensure sufficient reflection amplitudes. We further constrain the distance from $100°$ to $160°$ to minimize the interferences from *ScSScS* (Shearer, 1993; Schmerr and Garnero, 2006) and topside reflections from upper mantle discontinuities. After deconvolving the instrument responses, we apply a Butterworth bandpass filter with corner periods at 15 s and 75 s to the transverse component seismograms. We eliminate all traces with signal-to-noise ratios (SNR) less than 4.0 according to the definition of Gu et al. (2012), which is more restrictive than the majority of earlier studies due to a substantially larger data volume. The filtered seismograms are then inspected visually to eliminate duplicate records
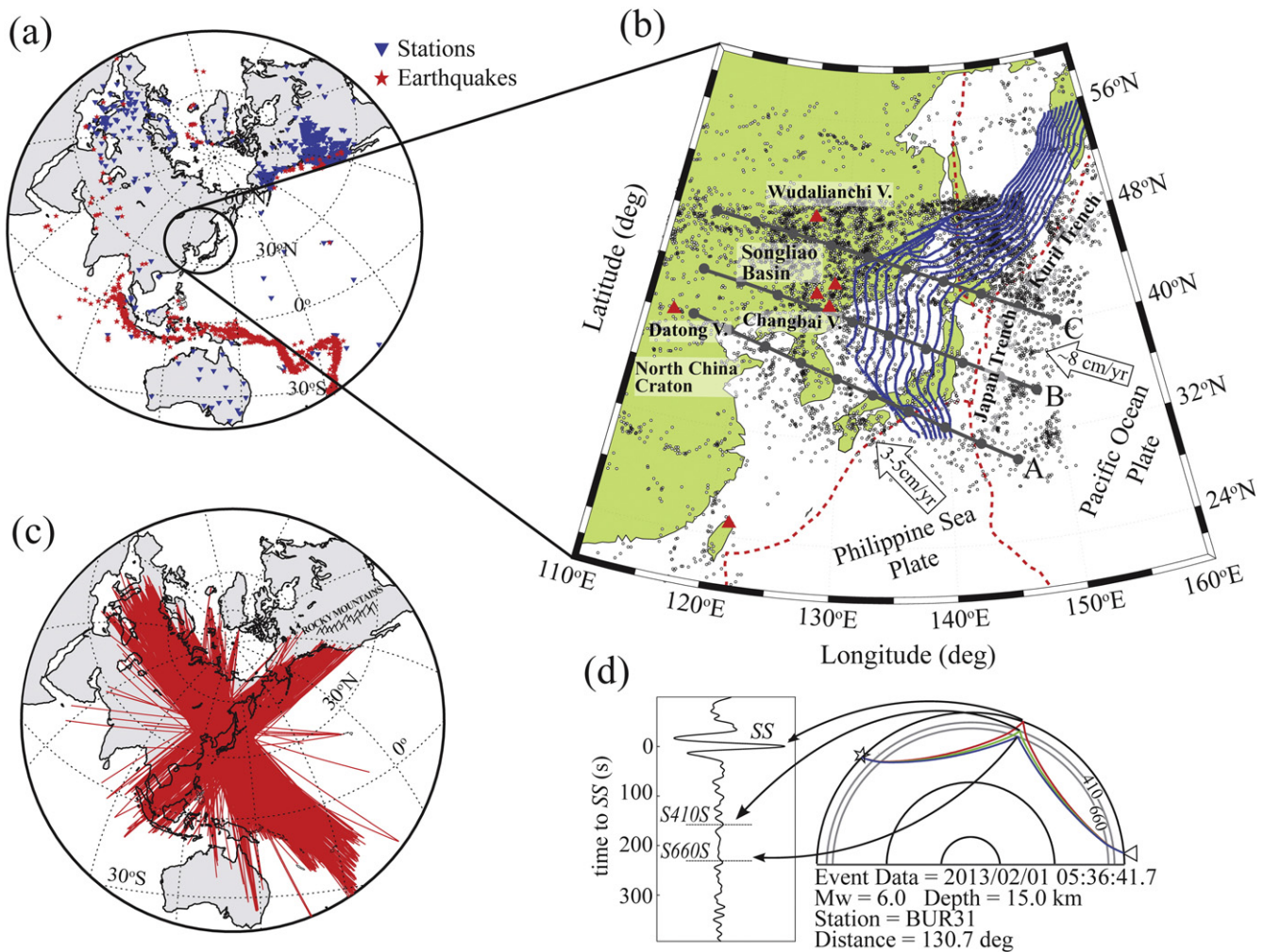

Fig. 1. (a) Global distribution of the earthquake (red stars) and station (blue triangles) locations used in this study. (b) The locations of *SS* bouncepoints from the earthquake-station pairs. The convergent plate boundaries and slab contours are indicated by the red and blue lines, respectively. The contour lines are taken at constant intervals of 50 km starting at 100 km depth (Hayes et al., 2012). The *SS* precursor waveforms are stacked into 30 bins along three parallel profiles A, B and C. (c) Path coverage of the *SS* precursors used in the stacking and inversion procedures. (d) A graphical representation of the theoretical ray paths of *SS* and its precursors for a source-receiver distance of 130.7°. The left panel shows an observed seismogram aligned on the maximum amplitude of *SS*. *S410S* and *S660* are marked based on the predicted arrival times from PREM (Dziewonski and Anderson, 1981).

or overlapping events (Schmerr and Garnero, 2006), and a polarity reversal is performed if necessary. This refined dataset contains 7868 waveforms from 1301 events. The densities of earthquakes and stations are particularly high in the southern and northern hemispheres, respectively (see Fig. 1a).

The amplitudes of SS precursors, which are comparable to those of noise, are greatly enhanced through stacking after aligning the waveforms on the first major swing of SS and normalizing each seismogram with respect to the peak amplitude of SS. We then deconvolved SS from the transverse component seismograms to minimize the source effects. To correct for the move-out we apply a constant time shift to each waveform based on the differential time between the predicted SS-S410S (Dziewonski and Anderson, 1981) and the reference time for a source-receiver distance of 130˚ (Gu and Sacchi, 2009). The move-out corrected seismograms are then time shifted to account for variations in crustal thickness and surface topography using CRUST1.0 (Laske et al., 2013) and ETOPO1 (Amante and Eakins, 2009), respectively. Finally, the time-shifted seismograms are sorted into common midpoint (CMP) circular bins (Shearer, 1991; Gu et al., 2012) along three parallel great-circle transects (profiles A to C) with 3˚ inline spacing (see Fig. 1b). Circular bins with a radius of 2˚ (approximately 15% overlap between two adjacent bins in the inline direction) are adopted to prevent over-smoothing while ensuring a sufficient number of traces in each bin for noise suppression. The stacked seismogram in each cap is calculated as the weighted sum of the time-corrected seismograms (Gu and Sacchi, 2009). It is worth noting that the majority of the source and receiver locations do not overlap with those of the topographic anomalies, e.g. the Rocky Mountains, Alps and Apennines, that may cause confounding observations within the MTZ (Fig. 1c). Moreover, while the azimuthal distribution is dominated by two perpendicular orientations (NE, NW), the crossing ray segments effectively average out the path heterogeneity and enable a reasonable recovery of the velocity and discontinuity depth in most bins (Zheng and Romanowicz, 2012).

2.1. Nonlinear waveform inversion

A potential pitfall during an SS precursor analysis is the velocity-discontinuity depth trade-off, as the timing of the secondary reflections is corrected based on relatively smooth shear velocity models obtained from earlier studies of body and/or surface waves. An improvement was proposed by jointly inverting for velocity and discontinuity depth using travel times (Gu et al., 2003) and multiple waveforms (Lawrence and Shearer, 2006a). In this study we quantitatively investigate the waveform information of an SS precursor dataset sampling the northwestern Pacific region. We model the full waveforms of SS precursors using the Genetic Algorithm (GA), an effective nonlinear inversion technique (Stoffa and Sen, 1991; Haupt and Haupt, 2004). A similar waveform inversion approach was recently utilized to analyze P-to-S converted phases (Chen et al., 2015) for imaging the continental crust.

As a proof of concept we first apply nonlinear inversions to a synthetic seismogram computed using GEMINI 2.2 (Friederich and Dalkolmo, 1995). The Green's function calculation assumes a spherically symmetric Earth model and uses a frequency domain method to numerically solve a system of ordinary first-order differential equations (Friederich and Dalkolmo, 1995; Friederich, 1999; Fichtner and Igel, 2008). We then utilize GA, a global optimization approach simulating the process of natural evolution (Haupt and Haupt, 2004), to explore solutions of mantle velocity and discontinuity depths that match the simulated waveform with 10% Gaussian noise. This binary-coded algorithm defines variables as indices to a regular discrete search space. Every model parameter (discontinuity depth and velocity perturbations) is represented by a binary string, while the inversion attempts to minimize the following cost function by adjusting the model parameters:

$$J = ||\mathbf{W}(\mathbf{d}_{obs} - \mathbf{d}(I\,\hat{\mathbf{m}}))||_2^2 + \mu ||\mathbf{D}I\,\hat{\mathbf{m}}||_2^2. \tag{1}$$

The symbol I is the interpolation operator sampling the model $\hat{\mathbf{m}}$, consisting of shear wave velocities at discontinuities, at a constant depth interval and $\mathbf{D}$ is a discrete approximation to the first-order derivative. The symbols $\mathbf{d}_{obs}$ and $\mathbf{d}(I\hat{\mathbf{m}})$ represent the observed and synthetic seismograms, respectively, and $\mathbf{W}$ is the weighting matrix. Finally, μ is a regularization parameter that controls the trade-off between the first and second terms (i.e., misfit and model norm, respectively); it is determined through trial and error. Our model solution consists of 6 layers, ranging from 220 km to 720 km along the depth axis, and the average spacing is 83.3 km. The S velocity is allowed to vary by ±4% from PREM, which is larger than the frequently reported range below the lithosphere — the primary target of this study (Grand et al., 1997; Mégnin and Romanowicz, 2000; Fukao et al., 2001; Gu and Dziewonski, 2002; Gu et al., 2003; Zhao et al., 2004; Obayashi et al., 2006; Li and van der Hilst, 2010; Ritsema et al., 2011). Due to the interference of crustal phases and the side-lobes of the main SS arrival, we mainly target the waveforms corresponding to the structure below 200 km. Our experiments suggest that an average of 1.5% shear velocity perturbation in the shallow mantle (above 220 km), which is comparable to the reported value beneath NE China (see Simmons et al. (2010) and Tang et al. (2014)), can cause a 2 km movement on the MTZ discontinuity depths and a perturbation of 0.01 km/s (or less) on the MTZ velocity. Neither artifacts are significant enough to alter the main observations of this study.

We fix the ratio between density and shear velocity based on PREM, and the perturbations in density are continuously updated as shear velocities vary during the inversions; a subjective choice that scales between velocity and density is adopted to reduce the computational cost (Marone et al., 2007; Yuan and Romanowicz, 2010; Liu and Gu, 2012). In general, the arrival times are highly sensitive to velocity and discontinuity depth, whereas the amplitude information embedded in the waveforms constrains both velocity and density. While density plays a minor role due to the strong dependence of the objective function on the phase/timing information, a reasonable input density model (PREM in this study) helps stabilize the solutions, especially the shear velocities.

Fig. 2 shows the results of the nonlinear inversion based on the synthetic data with 10% Gaussian noise. Our input model is modified from PREM, which consists of a low velocity layer atop the 410 and a high velocity layer at the base of the MTZ. We allow 120 solutions in each generation to ensure diversity at a manageable computation cost and steer clear of local extrema. The input and recovered models (see Fig. 2b) exhibit only minimal deviations, which are mainly associated with the discretized, relatively coarse, model space. The evolution history suggests almost immediate convergence to the final model from an initial suite of random models (Fig. 2d).

3. Result

3.1. SS precursor amplitude

Stacks of SS precursor waveforms show robust reflections off the 410 and 660 (S410S and S660S, respectively) within a laterally varying upper mantle beneath the northwestern Pacific region. To evaluate the standard errors and robustness of the SS precursors, we adopt a bootstrap resampling algorithm (Efron and Tibshirani, 1991; Shearer, 1993; Sacchi, 1998; Deuss, 2009) that makes automatic measurements from 200 randomly selected subsets of the data. During each trial, the amplitudes of S410S and S660S are directly determined from the positive peaks associated with the precursors. The amplitude uncertainties of the secondary arrivals are subsequently estimated from the standard deviation of the bootstrapped measurements (Deuss, 2009). Overall, the maximum standard error in amplitude is 0.2% based on bootstrap resampling.

We construct interpolated reflectivity maps from the S410S and S660S amplitudes (Fig. 3a and b), which are defined as the maximum
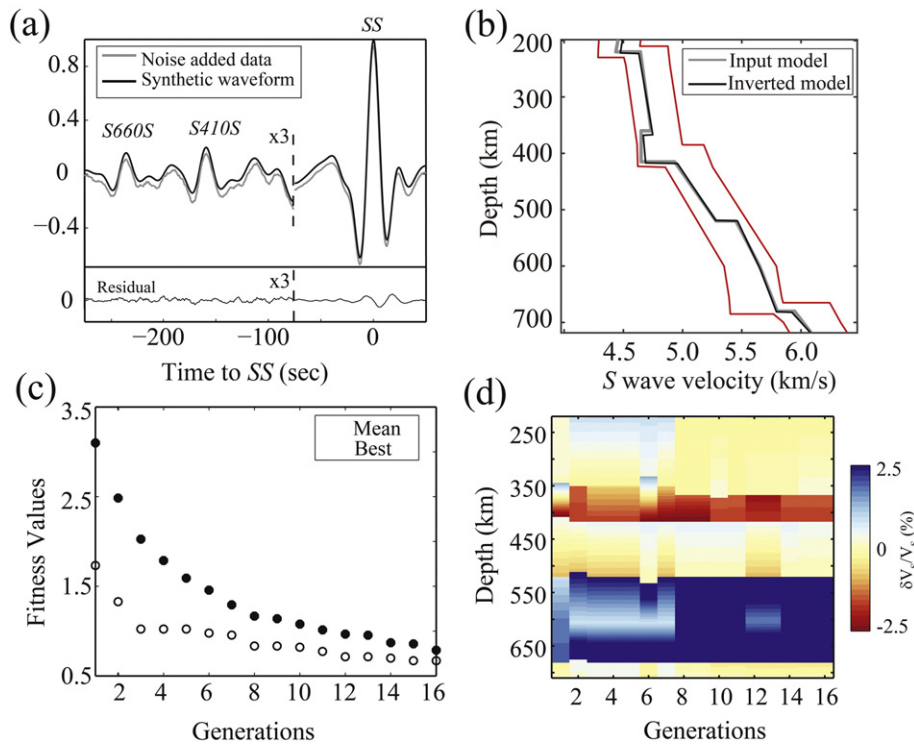
Fig. 2. (a) An input transverse component seismogram with 10% noise (gray) and the inverted trace after 15 generations (black). The precursors are magnified by a factor of 3 and the difference (data-synthetic) seismogram has been offset by −0.08 for clarity. (b) The input (gray) and recovered (black) model velocities. The red lines indicate the lower and upper boundaries of the model space. (c) The best and mean values of the objective function in each generation. (d) Color-coded velocity output from nonlinear inversions of the noise-added synthetic seismogram. Random input velocity structures are assumed in the first generation. (For interpretation of the references to color in this figure legend, the reader is referred to the web version of this article.)

amplitudes within 30 s time windows centered on the PREM predicted arrival times of these phases. Large-scale low and high reflectivity zones are detected at the top of the MTZ (see Fig. 3a). A SW–NE trending high reflectivity zone is present landward from the Wadati-Benioff zone, extending from the North China Craton to the Wudalianchi volcanic center and reaching the maximum value of ~7% (amplitudes are normalized with respect to the SS phase amplitudes) beneath the Changbai hotspot (see Fig. 3a). A second reflectivity zone is observed to the ocean side of the subducting Pacific plate, approximately 500 km away from the Japan trench. The centers of these two anomalies are approximately 1500 km apart.

Strong S660S reflections are also observed in the vicinity of the Wadati-Benioff zone (see Fig. 3b). The largest S660S, which attains ~8% of the SS amplitude, is identified within the reported slab contours (Hayes et al., 2012). While some of the amplitude variations may be affected by the data uncertainties (Fig. 3c and d), especially in the southern part of the study region due to low data density, the largest amplitudes of S410S and S660S are resolved to 95% confidence levels.

In comparison with PREM, which suggests respective reflection amplitudes of 3.9% and 6.1% relative to SS at a source-receiver distance of 130° for S400S and S670S, the observed values are 1.6–2.3 times higher beneath China (the former) and the Japan Basin (the latter). Part of the amplitude may be affected by the differential attenuation (Q factor) between SS and its precursors. However, our experiment based on conservative choices of Q values suggests a contribution no greater than 0.15%, well within the measurement uncertainties (see supplementary material).

3.2. Shear velocity variation

We perform nonlinear waveform inversions to simultaneously recover the shear wave velocities and depths of the upper mantle discontinuities. Following the steps of the iterative forward modeling procedure described in Section 2.1, the SS precursor waveforms are inverted based

on 15 generations each of which contains 120 simulated waveforms computed based on parallel programming. For consistency, the synthetic waveforms are filtered between the same corner periods as the observed data and the source mechanism is removed by isolating and deconvolving SS (Fig. 4). In general, the waveforms of S410S and S660S are accurately modeled by the synthetic seismograms, especially in view that 1) PREM contains no velocity and density jumps at mid MTZ depths (Dziewonski and Anderson, 1981), causing slight mismatches of the waveforms between S410S and S660S, and 2) the expected misfit between the data and synthetics is nonzero due to the uncertainties (e.g., random noise and imperfect structural corrections) in precursor amplitude and arrival time. The 520 km discontinuity (for short, the 520) is locally enhanced within the Wadati-Benioff zone (Gu et al., 2012), though its lateral variations are complex in all three cross-sections (see Fig. 4).

We determine a local 1D velocity model for each cap based on the stacked SS precursor waveform. A 3D model of the study region is then constructed from the resultant 1D models using a linear interpolation algorithm. The inverted shear velocities under NE China and the northwestern Pacific subduction regions (Fig. 5) highlight the morphology of the Japan-Kuril trench, showing an average velocity in excess of 1.5% relative to PREM. This high velocity structure intersects the base of the upper mantle near the Sea of Japan and extends westward toward Central Asia. Its presence and the contrasting discontinuity topography of the 410 (elevated by 10–25 km) and 660 (depressed by 10–27 km) are required to match the low amplitude precursory arrivals (see Figs. 3 and 4). The presence of a high velocity anomaly (cold subducting oceanic lithosphere) within the MTZ can reduce the impedance contrast across the 660 and produce low S660S amplitudes (see Figs. 4 and 5). The eastern side of this dipping high velocity structure shows a distinct low velocity zone, reaching its minimum value (approximately 1.5% slower than that of PREM) within the MTZ beneath the NE Honshu arc. The presence of this anomaly is required by a high amplitude, early-arriving S410S oceanward of the subducting Pacific plate (see
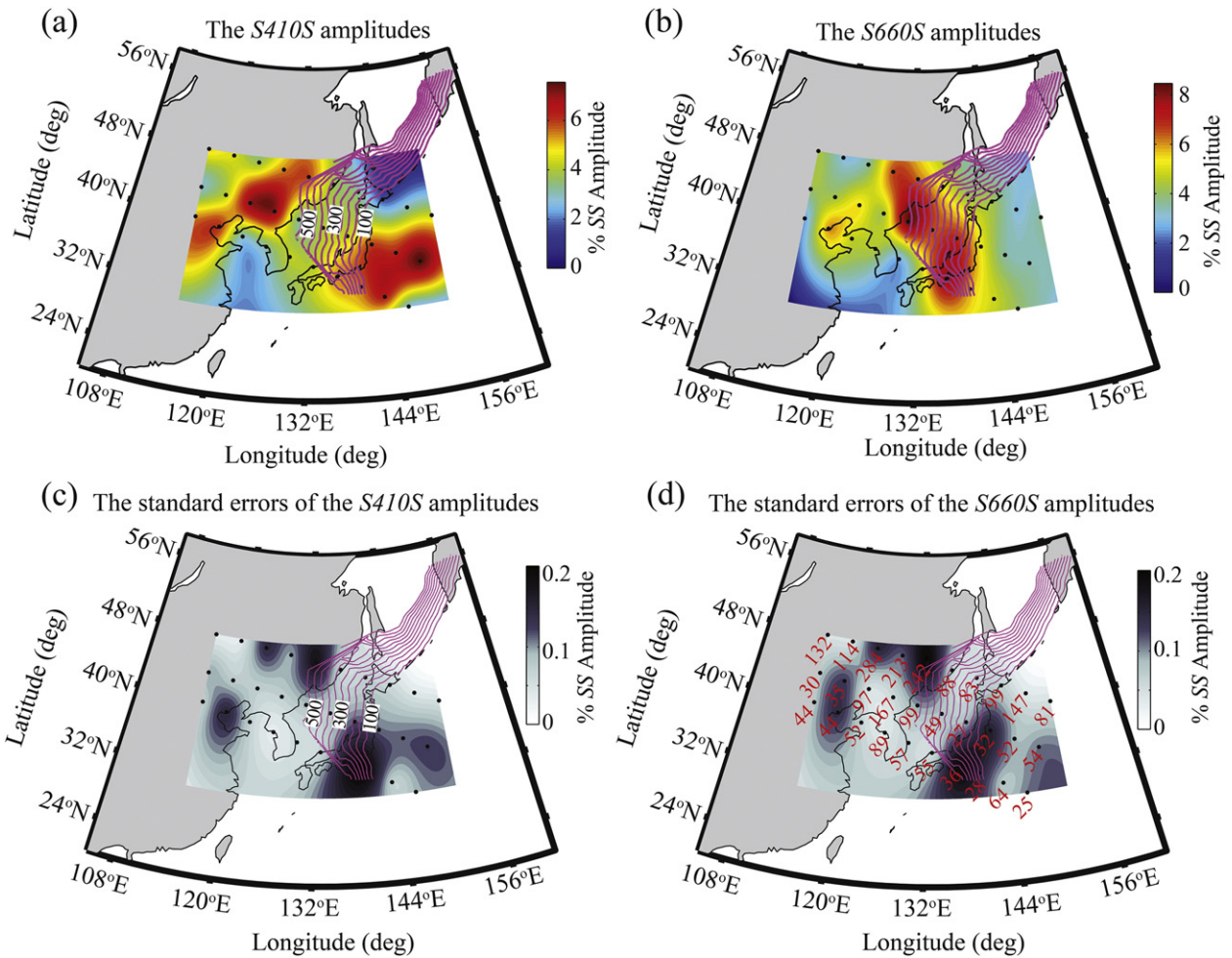
Fig. 3. The interpolated reflection amplitude maps of *S410S* (a) and *S660S* (b). (c) and (d) show the standard errors of the reflection amplitudes based on a bootstrapping analysis. The solid circles denote the centers of the averaging bins and the magenta lines show the slab contours (Hayes et al., 2012). The numbers at the center locations of the averaging bins in panel (d) indicate the data fold.

Figs. 3 and 4), which is partially accommodated by a relative depression (~15 km) of the 410. This low velocity structure appears to continue to the base of the MTZ under the Japan and Ryukyu trenches.

The most intriguing low velocity zone is observed in the upper mantle beneath NE China, potentially extending 1000 km further inland from the eastern end of the Wudalianchi volcanic belt to the northwestern facade of the Greater Hinggan Mountains (see Fig. 5a and b). The center, and the deepest part, of this broad anomaly resides beneath the Changbai Mountain Range, initiating at shallow depths and persisting down to a depth of ~500 km (see Fig. 5a–c). This low velocity structure is accompanied by a 5–10 km depression of the 410, which reflects an increased *SS-S410S* differential time in this region (see Fig. 4). The observed low velocity structure under the Wudalianchi volcanic field is limited to depths above 350 km, which is significantly shallower in comparison with that beneath the Changbai hotspot.

Changes in MTZ thickness across the study region, which are calculated from the inverted discontinuity depths (Fig. 6a), are consistent with those of Gu and Dziewonski (2002) using a correlation based method (Fig. 6b). Both studies show increased MTZ thickness north of the Ryukyu trench and beneath the Songliao Basin, especially in the present study where values exceed the global average of 242 km (Gu et al., 1998; Gu and Dziewonski, 2002; Lawrence and Shearer, 2006b). The largest difference, which reflects improvements in methodology and spatial resolution, is an anomalously thick MTZ in this study beneath NE China due to a 25–30 km depression of the 660 (see Z1 in Fig. 6a). This anomaly is consistent with the recent findings

of Liu et al. (2015) based on migrated receiver functions (see the dashed-line box, Fig. 6a). To a lesser extent, the MTZ beneath the Ryukyu trench is approximately 15 km thicker in this study than Gu and Dziewonski (2002), despite similar shapes and signs (see Z2 in Fig. 6a).

As will be discussed in Section 4, the combination of a depressed and amplified 410, a severely deformed 660 and a low velocity asthenosphere beneath the Changbai-Wudalianchi hotspot has major implications for the intraplate volcanism in NE China.

4. Discussion

4.1. General assessment

This study presents a nonlinear optimization method that accurately determines the large-scale mantle shear velocity and discontinuity topography based on *SS* waveform information alone. In comparison with a recent study of *SS* precursors for the same region by Gu et al. (2012), the current study benefits from denser data coverage, especially in the northern flank of the study region where data density increased by ~50% due to four extra years of recordings. The resolution improved further from the *SS* precursor amplitude information, which is essential in resolving the impedance contrast at major seismic discontinuities, as well as from the reduced trade-off between velocity and discontinuity depth. While the scale of the reported features (>300 km) may be smaller than the nominal resolution (>1200 km), the use of multiple
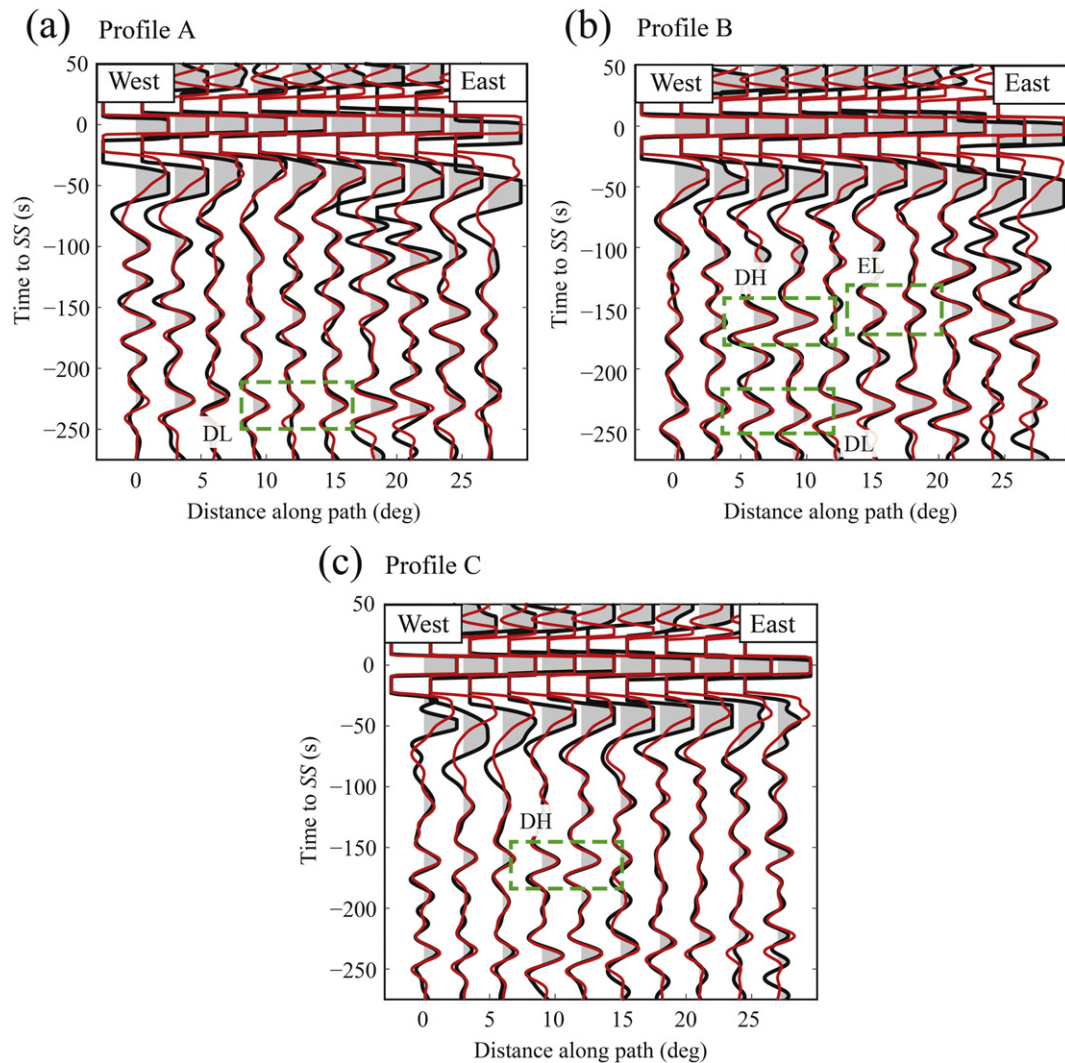
Fig. 4. SS precursor waveform inversion results for profiles A to C. In all panels the black and red lines show the observed and synthetic stacks, respectively. The key features in the waveform data are highlighted using the dashed boxes. The symbols D and E represent areas with depressed (former) and elevated (latter) discontinuity topography. The letters H and L indicate the high and low amplitude precursory arrivals, respectively. (For interpretation of the references to color in this figure legend, the reader is referred to the web version of this article.)

stations (Rost and Thomas, 2009; Schmerr and Thomas, 2011) and dense sampling (Cao et al., 2011; Gu et al., 2012; Zheng and Romanowicz, 2012) can significantly reduce the effective Fresnel zone and smearing along an isochron (Rost and Thomas, 2009; Cao et al., 2010).

The westward dipping high velocity structure beneath the back-arc region (Fig. 7a-c), which is consistent with earlier findings from P and S-wave travel time (van der Hilst et al., 1991; Fukao et al., 1992; Gorbatov and Kennett, 2003; Huang and Zhao, 2006; Obayashi et al., 2006; Li and van der Hilst, 2010; Zhao et al., 2012) and waveform (Mégnin and Romanowicz, 2000; Friederich, 2003) inversions, has been widely associated with the subducted Pacific lithosphere beneath the Japan and Kuril islands. The general morphologies of the high velocity structures are concordant with those of Obayashi et al. (2006) (see Fig. 7d–f), both of which are well supported by the locations of deep focus earthquakes in the study region.

The fate of the subducted Pacific plate has been a source of considerable debates (van der Hilst et al., 1993; Grand, 2002; Huang and Zhao, 2006; Schmerr and Thomas, 2011). While relatively unimpeded penetration into the lower mantle has been documented along the Mariana (Creager and Jordan, 1986; Bijwaard et al., 1998; Zhao et al., 2004;

Huang and Zhao, 2006; Li et al., 2008) and Kuril (Jordan, 1977; Li et al., 2008; Schmerr and Thomas, 2011; Gu et al., 2012) islands, substantial deformation and changes in slab dip have been frequently suggested at the base of the upper mantle as evidence of slab deflection or bending (Zhao et al., 2004; Fukao et al., 2001; Huang and Zhao, 2006; Gu et al., 2012). Beneath the Sea of Japan, the seismic structure in the MTZ is dominated by a 1.5–2.0% increase in P velocity (Fukao et al., 1992; Huang and Zhao, 2006; Obayashi et al., 2006), but the deflected slab segment is less well imaged by shear velocities across the study region (Gorbatov and Kennett, 2003; Fukao et al., 2009). The result of our waveform inversion of SS precursors provides further evidence for the slab deflection below the Sea of Japan and stagnation beneath eastern China (see Fig. 7a–c).

4.2. MTZ structure and dynamics

The simultaneous solutions of velocity and discontinuity depth enable a detailed examination of the effective mantle temperatures within the MTZ (Schmerr and Garnero, 2006). On the global scale, the depths of the 410 and 660 are either uncorrelated (Flanagan and Shearer, 1998; Gu et al., 1998) or slightly anticorrelated (Revenaugh and Jordan,
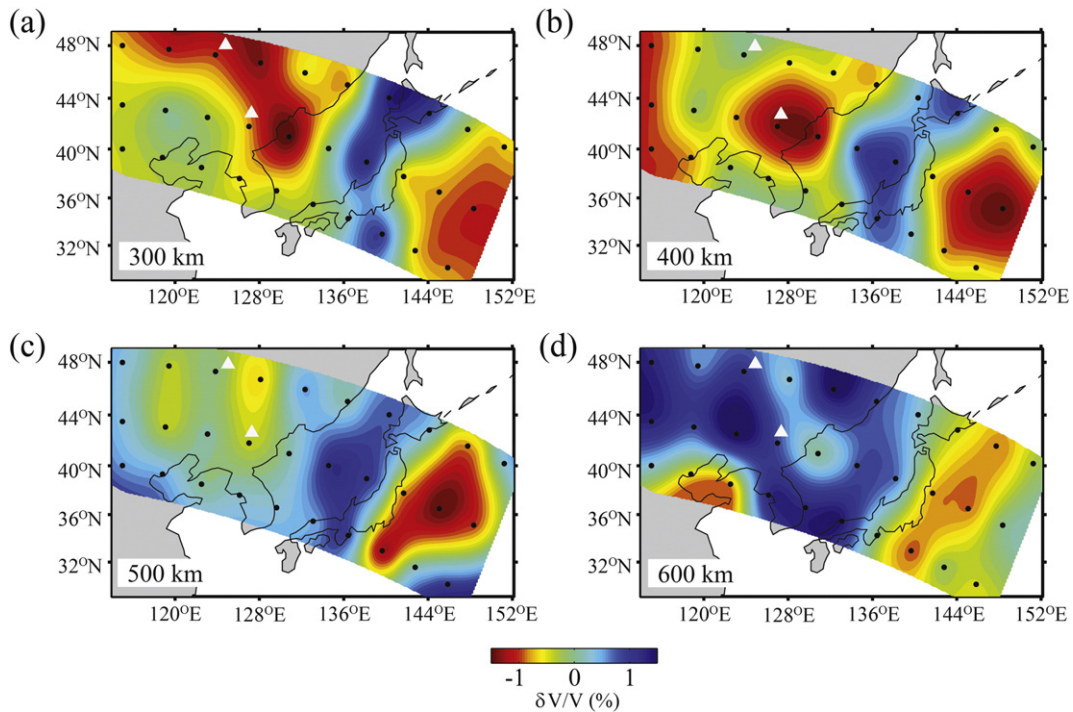
Fig. 5. Lateral variations in *S*-wave velocity relative to PREM (Dziewonski and Anderson, 1981) at 300 km (a), 400 km (b), 500 km (c), and 600 km (d) depths beneath NE China and the northwestern Pacific region. The blue and red colors represent fast and slow anomalies, respectively. The solid circles mark the centers of the averaging caps and the white triangles denote the locations of major intraplate volcanoes. (For interpretation of the references to color in this figure legend, the reader is referred to the web version of this article.)
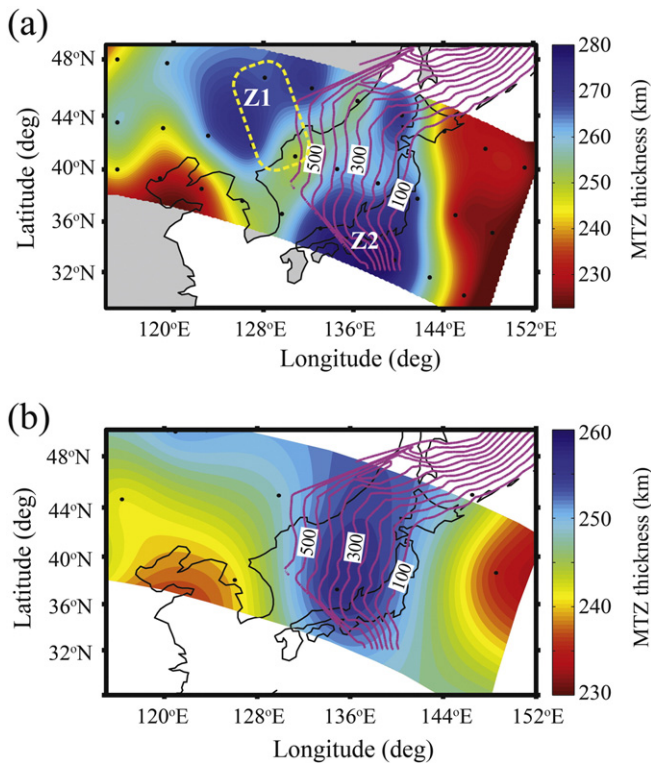

Fig. 6. (a) MTZ thickness variations inferred from the inverted depths of the 410 and 660 from this study. (b) MTZ thickness variations reported by Gu and Dziewonski (2002). The red and blue colors represent regions of narrow and thick MTZ, respectively. Z1 and Z2 indicate anomalously thick MTZ beneath NE China and the Ryukyu trench, respectively. The dashed-line box in panel (a) outlines a relatively thick MTZ (>270 km) in Liu et al. (2015), obtained from depth migrated P-to-S converted waves. (For interpretation of the references to color in this figure legend, the reader is referred to the web version of this article.)

1991; Gossler and Kind, 1996; Gu et al., 2003; Li et al., 2003). The lack of correlation is largely attributable to smaller-scale heterogeneities (Schmandt and Humphreys, 2010), compositional variations (Weidner and Wang, 1998; Schmerr and Garnero, 2007), or non-vertical structural geometry (Gu et al., 2012). Considerations for localized dipping thermal-chemical structures are crucial in these correlation analyses, especially in the vicinity of major subduction zones. To properly account for slab dip, we compute the correlation coefficients between MTZ thickness and the average MTZ shear velocity for slab dip angles ranging from 15 to 90°. The maximum correlation coefficient (0.72) from all three profiles is attained at 30°, which is 22% higher than the uncorrected (90° dip) value (Fig. 8). This effective slab dip is in excellent agreement with previously reported values (van der Hilst et al., 1993; Gudmundsson and Sambridge, 1998; Huang and Zhao, 2006; Hayes et al., 2012), which highlights 1) the need to properly consider the inclined slab morphology, and 2) the dominance of thermal, rather than compositional, variations within the MTZ. A closer examination of the correlation coefficient at the optimal slab dip (see Fig. 8c and d) suggests substantial improvements over the conventional vertical structure assumption in global analyses (Flanagan and Shearer, 1998; Gu et al., 1998; Tauzin et al., 2008; Houser and Williams, 2010). The strength of the correlation (0.72) largely reflects the severity of thermal perturbations, relative to the ambient mantle, within the subducting oceanic lithosphere. It is enhanced further by a dipping low velocity structure east of the Wadati-Benioff zone (see A5 in Fig. 7a and b), which has been previously reported by Obayashi et al. (2006) and Gu et al. (2012) in possible connection with 1) convective return flow in connection with slab dynamics (Bercovici and Karato, 2003; Ohtani et al., 2004), and 2) partial subduction of a residual Mesozoic hot thermal plume (Larson, 1991; Tatsumi et al., 1998; Honda et al., 2007).

4.3. Mantle beneath the Changbai-Wudalianchi hotspot

A notable seismic anomaly that reduces the anticorrelation between the depths of 410 and 660 is the low velocity zone beneath the
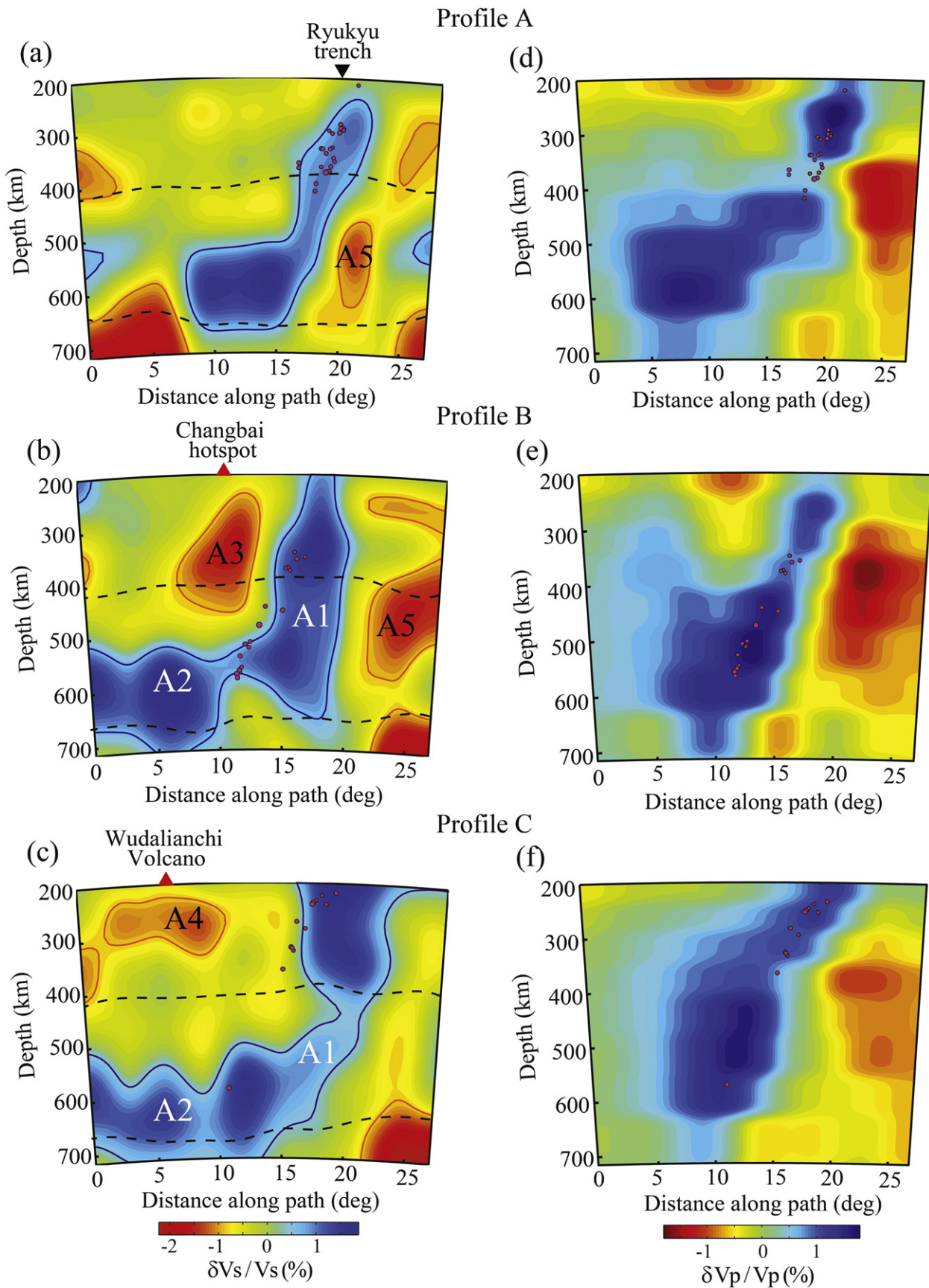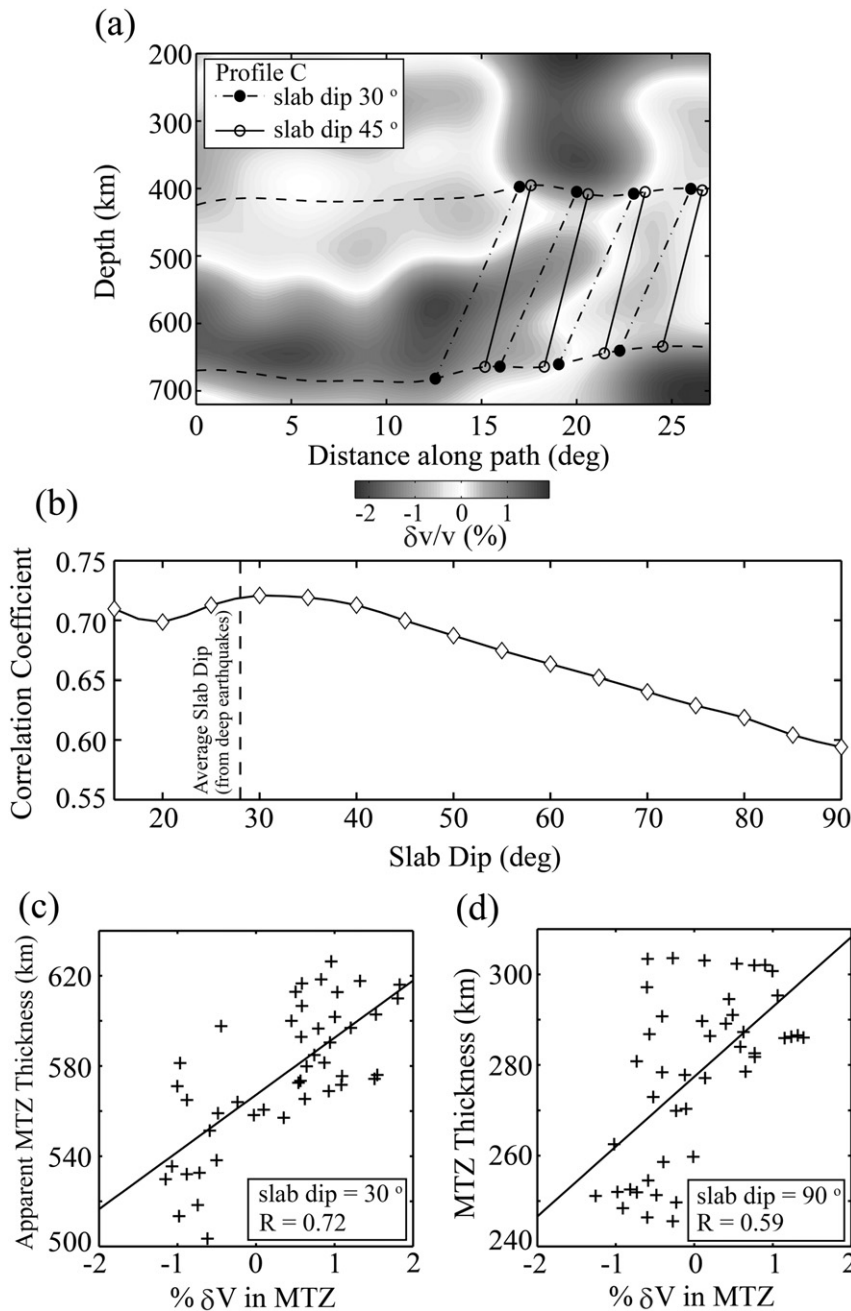
Fig. 8. (a) A cross-section of our shear velocity model along profile C. The dashed and solid straight lines indicate how the MTZ thickness and average MTZ velocity are measured along the slab dips of 30 and 45°, respectively. (b) Correlation between MTZ thickness and the average MTZ shear velocity perturbations at a range of dip angles. (c) Observations of apparent MTZ thickness versus the apparent average MTZ shear velocity along a slab dip of 30°. The least-square fit and correlation coefficient are also shown. (d) Similar to (c) but for a slab dip of 90°.

Changbai-Wudalianchi hotspot. The geometry of this low velocity structure (see A3 and A4 in Fig. 7b and c) is in excellent agreement with those from earlier studies of this proposed back-arc region (Tatsumi et al., 1990; Lei and Zhao, 2005; Huang and Zhao, 2006; Li and van der Hilst, 2010; Tang et al., 2014). This anomaly has been linked to the horizontally deflected Pacific slab and the subsequent upwelling of hot asthenospheric material (Tatsumi et al., 1990; Li and van der Hilst, 2010; Zhao and Liu, 2010), though more recent studies (Tang et al.,

2014; Liu et al., 2015) have suggested a slab gap west of the stagnant slab.

In this study, the depressed 410 and 660 beneath the Changbai and Wudalianchi volcanic fields imply discontinuous seismic velocities within the MTZ (see A2 in Fig. 7b and c), above which a low velocity structure (see A3 and A4 in Fig. 7b and c) continues to the shallow mantle (Fig. 11). Anomaly A3 appears to terminate at mid-MTZ depths (~500 km), which is moderately deeper than the earlier estimates

Fig. 7. (a)–(c) West–east vertical cross-sections of the inverted shear wave velocity anomalies along profiles A to C from 200 to 720 km depths beneath the northwestern Pacific subduction zones and NE China. The magenta circles indicate the locations of deep earthquakes within a 2° distance from each profile. The depths of the 410 and 660 are indicated by the dashed lines. A1 and A2 mark the downgoing and stagnant parts of the Pacific slab, while A3 and A4 denote low shear velocity anomalies beneath the Changbai-Wudalianchi hotspot. A5 highlights the low seismic velocities on the ocean side of the Wadati-Benioff zone. (d)–(f) Similar to (a)–(c), but for an earlier model of P-wave velocities (Obayashi et al., 2006).

(Zhao and Ohtani, 2009; Li and van der Hilst, 2010). Judging from the MTZ velocity characteristics, the transition from low to high velocity appears to be gradational rather than abrupt. The presence of the low velocity zone does not significantly impact the amplitude of the 520, which is diffuse above the stagnant part of the Pacific slab (see Figs. 4b and 7b).

To examine the robustness and resolution of mantle velocities and discontinuity depths, we conduct a hypothesis test, a frequently adopted technique for linearized inversions. In this test we introduce a low velocity structure resembling that beneath the Changbai hotspot (Fig. 9). This hypothetical anomaly terminates near 410 km, overlying a high velocity structure similar to the stagnant oceanic lithosphere. The input depths of the 410 and 660 are both depressed by more than 10 km near the largest shear velocity perturbations. After the synthetic seismograms are computed for each cap location based on these input parameters, we add up to 0.2% Gaussian noise depending on the observed standard errors from bootstrap resampling (Section 3.1). The recovered models through the same inversion procedure show two well-defined seismic velocity anomalies with the same signs and shapes as the input (see Fig. 9). The maximum amplitudes of the recovered anomalies are about 80% and 95% of the assumed values of the respective low

and high velocities; the recovery of the latter anomaly is superior due to a larger, more laterally coherent input structure. The amplitudes near the edges of the major anomalies are preferentially reduced due to the lateral averaging with a substantially weaker structure to the west. The depressions of the phase boundaries near the center of the profile are recovered to 90–95% relative to the input values. The performance of the inversion is equally effective in resolving a relatively shallow low velocity zone beneath the Wudalianchi hotspot. In this case, the inversion recovers over 75% of the maximum input velocity and discontinuity topography, as well as a minor lateral gradient east of the volcanic center (see Fig. 9). Our hypothesis test demonstrates that 1) a restoring resolution analysis is equally effective in nonlinear inversions as their linear counterpart, and 2) the morphologies of the low velocity zones beneath the volcanic centers and the underlying stagnant slab can be sufficiently resolved in our study region.

To further validate the recovered images from the 1D waveform inversions of SS precursors (see Fig. 7), we implement 2D waveform tomography using the same nonlinear inversion technique (Fig. 10). The mantle is discretized into cells of 3° (in the horizontal direction) by 50 km (in the vertical direction). To simplify this problem, we assume known discontinuity depths from the 1D inversions (see Fig. 7) and
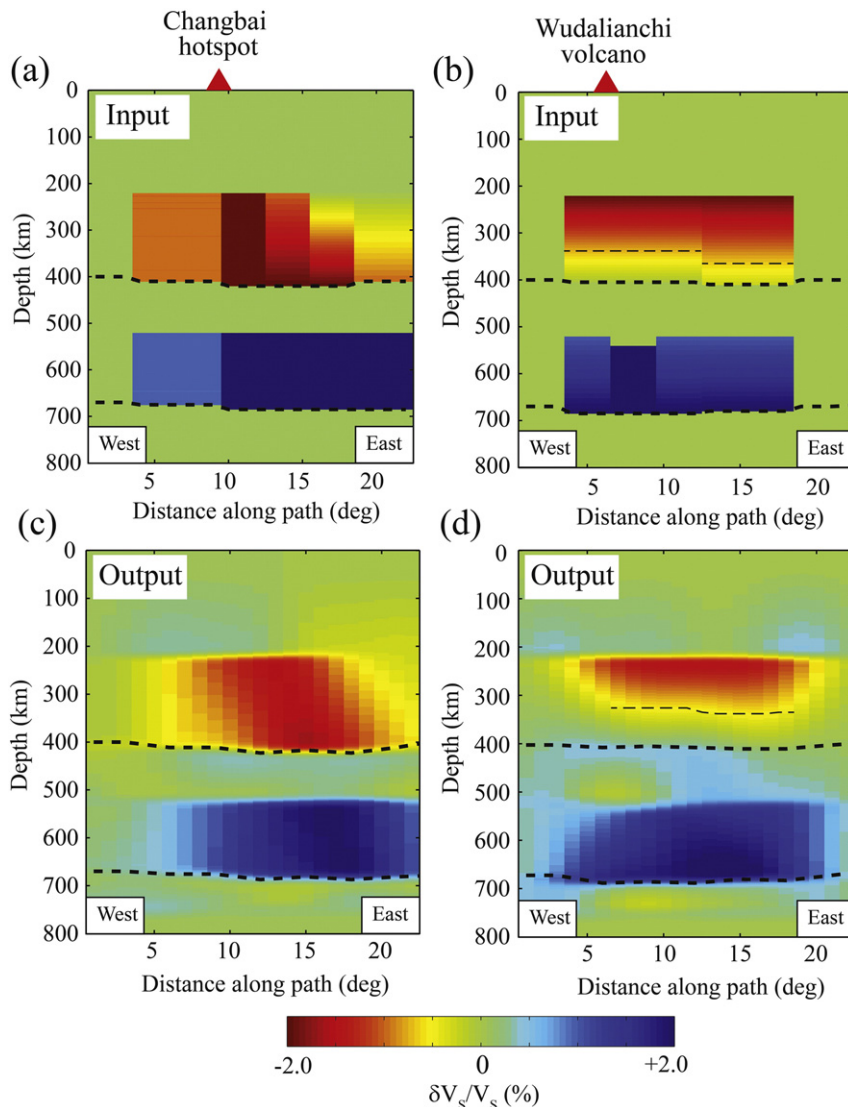

Fig. 9. Input models (panels a and b) and the inverted results (panels c and d) from a simulated recovery test. The depths of the 410 and 660 are indicated by the thick dashed lines (see Section 4.3 for details).

only solve for perturbations of shear velocities within each cell; it is worth noting that we define a finer vertical cell size of 10 km around the discontinuity depths of 220, 300, 400, 520 and 670 km. In this approach, the travel times of the precursors and their corresponding reflection coefficients are calculated using the 2D ray tracing method (Lebedev and Nolet, 2003; Zhao et al., 2004; Priestley et al., 2006; Lawrence and Shearer, 2006a). Then, the reflectivity profiles are convolved with the source time functions extracted from the stacked waveforms (Shearer et al., 1999). We generate over 2000 solutions at each generation, while 5% of the initial random solutions are replaced by the shear velocities from GyPSuM (Simmons et al., 2010). The optimized synthetic waveforms from 2D nonlinear inversions closely match the observations along profile B (see Fig. 10b). The velocity model shows a westward dipping structure similar to that recovered by the 1D waveform inversions, which appears to flatten toward NE China. The maximum velocity of the slab (1.5%) is comparable to that of the 1D inversion, whereas the low velocity zone above the 410 (−1.1%) is slightly weaker than the 1D counterpart. Part of the amplitude difference between the 1D and 2D inversion outcomes could be explained by the inclusion of a more realistic, low velocity lithosphere in the latter experiment.

Our models consistently suggest a relatively warm mantle in the vicinity of the 410. The observed 5–10 km depression of the 410 beneath the intraplate volcanic fields in mainland China can be attributed to the response of the olivine to wadsleyite phase transition, an exothermic reaction with a positive Clapeyron slope of 1.5–4.0 MPaK^{-1} (Akaogi et al., 1989; Houser and Williams, 2010; Lessing et al., 2014), to the presence of a high temperature anomaly above or across this boundary. By assuming the temperature dependence of the shear wave velocity ($\frac{\partial lnV_s}{\partial T} = {-7\times10^{-5}}/{K}$) for a dry upper mantle (Houser and Williams, 2010), an S wave velocity reduction of 1.5% results in an approximate temperature increase of 215 K relative to the average value of 1694 K for the olivine phase change (Houser and Williams, 2010). The phase boundary moves toward the higher pressures (by 320–860 MPa) and greater depths, which are consistent with recent reports of 20–30 km of depression in the same region (Li et al., 2000; Li and Yuan, 2003; Liu et al., 2015). Different mechanisms have been proposed to explain the origin of a widely distributed low velocity regime in the upper mantle beneath NE China, most of which are associated with the subducting Pacific plate. An incomplete list of these mechanisms include 1) partial melting induced by the deep dehydration of the slab (Zhao and Ohtani, 2009), 2) passive upwelling of asthenospheric material in response to slab accumulation within the MTZ (Bercovici and Karato, 2003; Kuritani et al., 2009; Faccenna et al., 2010), and 3) mantle upwelling from a slab gap (Tang et al., 2014; Liu et al., 2015).

The first mechanism infers significant amount of water near the 410, while up to 3 wt% water could be present in the MTZ (Bercovici and Karato, 2003). A relatively wet mantle around the 410 would elevate
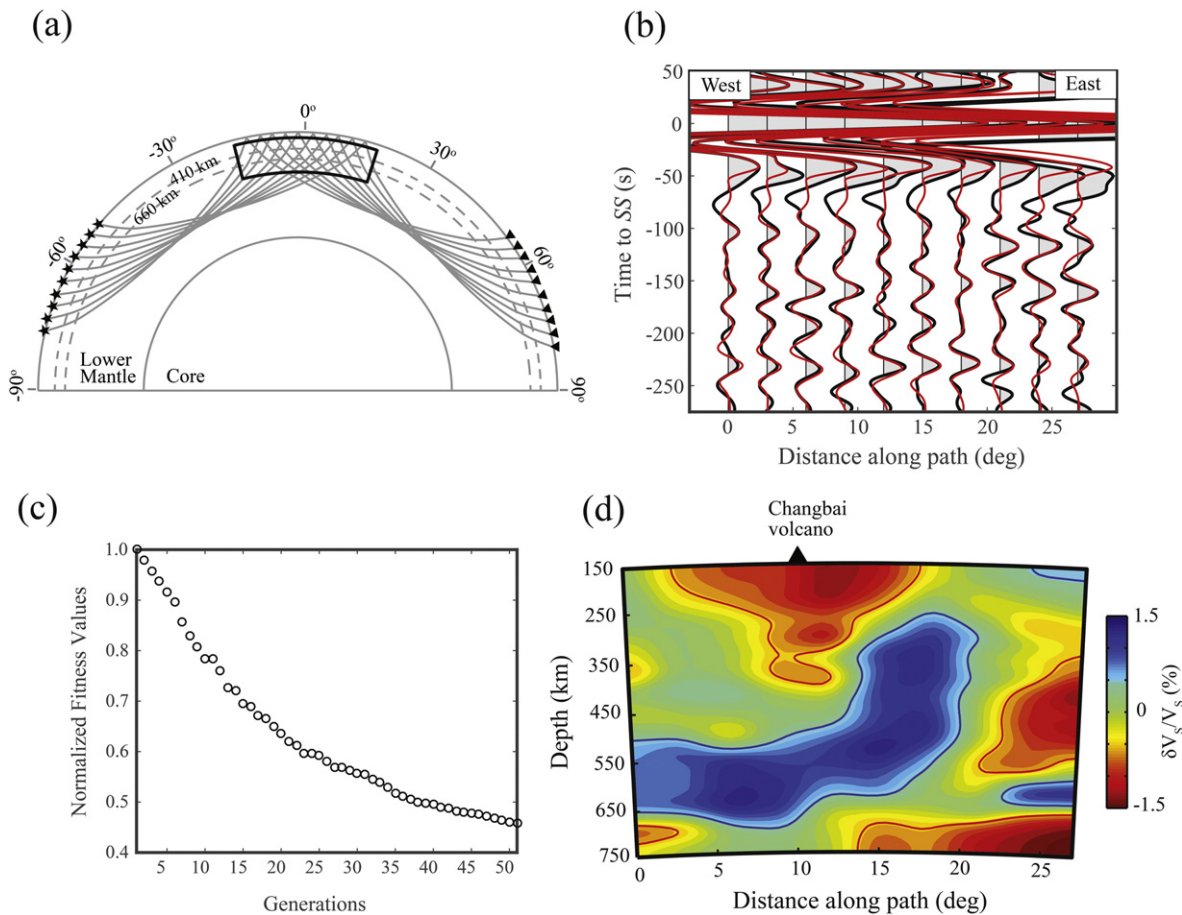

Fig. 10. 2D waveform tomography using the stacked waveforms from profile B (see Fig. 4). This model clearly shows a high velocity structure, which is associated with the subducting plate, and reduced shear wave velocities beneath NE China. (a) A schematic view of the SS ray paths used in the waveform tomography. The sources and receivers are indicated by stars and triangles, respectively. The thick black lines outline the area covered by the tomographic approach. The outlined area covers the depth range of 200–750 km. (b) The visual comparison between the observed (black) and synthetic (red) waveforms shows a good agreement between the input and modeled waveforms. (c) The normalized fitness values of the objective function in each generation. (d) Color-coded cross-section (outlined area in panel a) of the shear wave velocity perturbations. The blue and red colors represent the fast and slow velocities, respectively. (For interpretation of the references to color in this figure legend, the reader is referred to the web version of this article.)

the olivine to wadsleyite phase boundary. While the extent of the elevation in the presence of water remains questionable (Frost and Dolejš, 2007; Schmerr and Garnero, 2007), an elevated 410 is simply inconsistent with either the observed depression from this (see Fig. 7) and earlier studies (Li and Yuan, 2003; Liu et al., 2015), or the reported water content in this region (Ichiki et al., 2006; Chen et al., 2007; Fukao et al., 2009; Ye et al., 2011). In the case of water saturated mantle, a hydrous melt lens may form atop the 410 and produce multiple phase transitions. This was reported in South America where a relatively deep, modest wet to dry wadsleyite reflection was detected at 415 km (Schmerr and Garnero, 2007). Based on numerical experiments from the same study, the expected amplitude (which increases with water content) is significantly lower than the predicted value from PREM and far below those of our observations under the Changbai hotspot.

A favorable solution for the observed 410 amplitude and depth requires a significantly increased impedance contrast across a depressed 410, which could be satisfied by the presence of a melt layer in a relatively dry, warm mantle. Increasing the Mg content by up to 4% within the melt layer can effectively depress the 410 by approximately 10 km (Fei and Bertka, 1999; Schmerr and Garnero, 2007), which corroborates our observations in NE China. Both decompression melting associated with passive upwelling (Bercovici and Karato, 2003; Faccenna et al., 2010) and a significant sub-slab component from the slab window (Tang et al., 2014) can induce partial melting atop the 410. This melt layer would depress the 410 phase boundary, enhance the impedance contrast and substantially increase the *S* wave reflection amplitude, which are all supported by our observations beneath the Changbai hotspot. Insufficient resolution around the suggested slab window (see Figs. 7 and 11) makes it difficult to clearly differentiate between these two candidate mechanisms, however.

Further inferences could be made regarding the mantle beneath the two volcanic centers examined in this study. Despite the considerable depth difference between the Changbai (about 500 km) and Wudalianchi (about 350 km) hotspots, trace element analyses (Basu et al., 1991; Kuritani et al., 2009) suggest a comagmatic upper mantle origin with EM1 (Enriched Mantle 1) composition (Jackson and Dasgupta, 2008). Hence, it is conceivable that the mantle upwelling beneath the Changbai hotspot is responsible for the source of partial melt for both volcanic centers in view of its greater vertical extent and strength (see Figs. 5a and 11). Further work will be needed to quantify the accuracies of the aforementioned mechanisms and interpretations.

Finally, increased seismic velocities at the base of the MTZ under NE China and a deep 660 (>680 km) relative to the regional average of 655–665 km (Shearer, 1993; Gu et al., 2003; Houser and Williams, 2010) are consistent with the respective measurements based on analyses of receiver functions (Li et al., 2000; Li and Yuan, 2003; Liu et al., 2015) and migration of long period *SS* precursors (Gu et al., 2012). A maximum depression of 20–30 km is reported on the 660, possibly in association with a decrease of 300–400 K in MTZ temperature (Li and Yuan, 2003; Ye et al., 2011). A negative temperature anomaly of ~300 K and a greater depth of the 660 jointly suggest increased *S* wave velocities of ~ 2% in the presence of a negative Clapeyron slope from the post-spinel phase transition (Houser and Williams, 2010; Lessing et al., 2014). The low temperature anomaly and locally depressed 660 could be explained by the existence of water within the MTZ, the amount of which depends on the volume entrained within the slab as well as the residence time of the slab (Fukao et al., 2009). Recent *S* waveform modeling from NE China detects a 130 km thick high velocity zone at the base of the MTZ, which may contain up to 0.3 wt% water based on the estimates from Ye et al. (2011).

5. Conclusion

Our study demonstrates that the shear wave velocity and the topography of MTZ discontinuities beneath NE China and the northwestern Pacific region can be simultaneously recovered using the waveforms of *SS* precursors alone. A statistically significant positive correlation is observed between MTZ thickness and the average MTZ velocity along
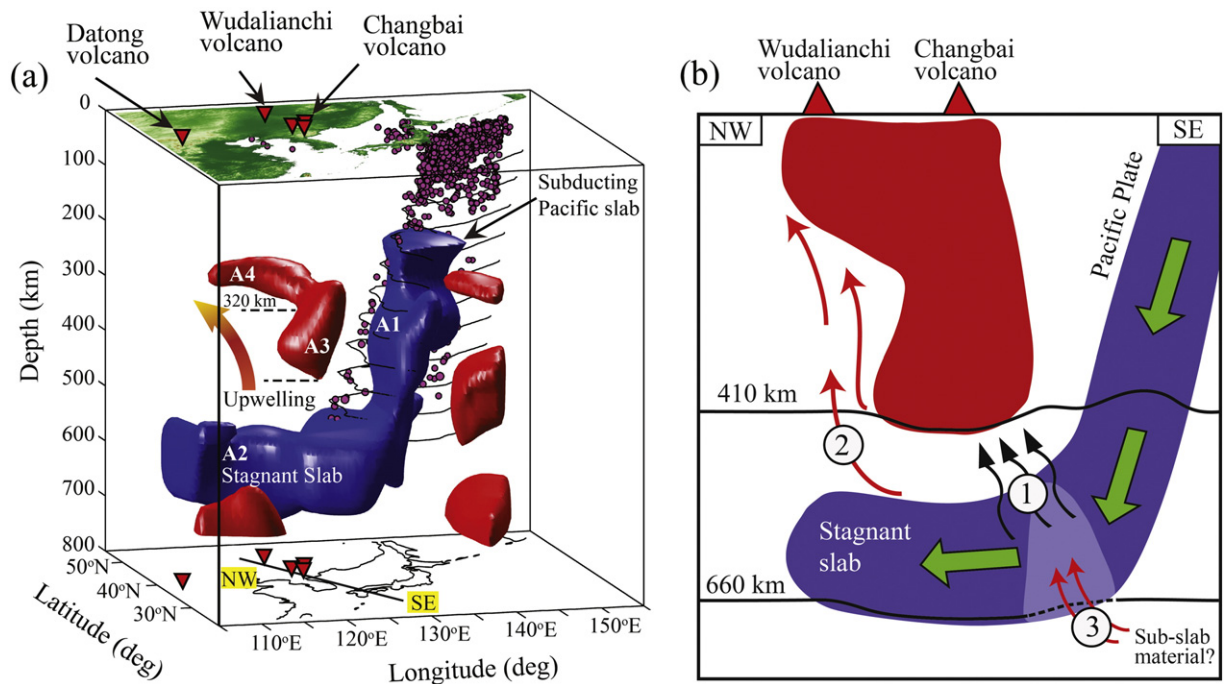

Fig. 11. (a) Isosurfaces showing the major seismic anomalies beneath NE China and the northwestern Pacific subduction zones in the depth range of 200 to 700 km. The blue and red colors represent the fast and slow shear velocities, respectively, at the corresponding isosurfaces of +0.65% and −1.0%. The definitions of major seismic anomalies (A1–A5) are the same as in Fig. 7. The black lines show the slab contours, which are taken at 50 km depth intervals starting at 100 km (Hayes et al., 2012), and the magenta circles indicate the locations of deep-focus earthquakes. (b) A schematic illustration of a NW-SE vertical section (see Fig. 11a), showing the possible origins of the intraplate volcanism in NE China. Three possible mechanisms of the intraplate volcanism (discussed in Section 4.3) are illustrated: (1) deep dehydration of the slab, (2) passive upwelling in response to the subduction of the Pacific plate, and (3) escaping hot sub-slab material through a slab window. (For interpretation of the references to color in this figure legend, the reader is referred to the web version of this article.)

an effective slab dip of ~30°, which reflects the dominant effect of thermal heterogeneity in the upper mantle and MTZ. A strong low velocity zone is found beneath the active volcanoes in NE China, persisting to a depth of ~500 km, which implies that the Changbai and Wudalianchi hotspots may be fueled by a hot thermal anomaly from MTZ depths.

Passive upwelling and/or a slab window could be responsible for a relatively water-poor melt layer atop the 410, which causes 5–10 km depression and substantially enhances the reflection amplitude on the olivine to wadsleyite transition. A distinctive low velocity structure is also observed east of the Wadati-Benioff zone, which narrows the MTZ by 30 km relative to its regional average. This low velocity zone is possibly associated with (i) a fossil superplume (~140 Ma) or (ii) upwelling hot mantle material in response to slab–lower mantle interaction. Overall, our findings from nonlinear *SS* precursor waveform inversions provide a new window into the effects and fate of the subducting oceanic plate in the northwestern Pacific region.

From a technical stand point, the nonlinear joint inversion technique introduced in this study represents a new phase in the retrieval of seismic properties pertaining to large scale thermal/chemical structures in the mantle. This is not aimed to be a replacement of the existing travel time and waveform tomographic approaches, especially in view of the relatively coarse spatial resolution of the *SS* precursor dataset, but an improvement that effectively incorporates the amplitudes of the secondary reflections or conversions from mantle interfaces.

Acknowledgment

Appendix A. Supplementary data

Supplementary data to this article can be found online at http://dx.doi.org/10.1016/j.gr.2016.07.006.

References

Akaogi, M., Ito, E., Navrotsky, A., 1989. Olivine-modified spinel–spinel transitions in the system Mg$_2$SiO$_4$–Fe$_2$SiO$_4$: calorimetric measurements, thermochemical calculation, and geophysical application. Journal of Geophysical Research 94, 15671–15685.

Amante, C., Eakins, B., 2009. ETOPO1 1 arc-minute global relief model: procedures. Data sources and analysis. NOAA Technical Memorandum NESDIS NGDC-24. National Geophysical Data Center, NOAA.

An, Y., Gu, Y.J., Sacchi, M.D., 2007. Imaging mantle discontinuities using least squares radon transform. Journal of Geophysical Research 112, B10303.

Anderson, D.L., 1967. Phase changes in the upper mantle. Science 157, 1165–1173.

Basu, A.R., Junwen, W., Wankang, H., Guanghong, X., Tatsumoto, M., 1991. Major element, REE, and Pb, Nd and Sr isotopic geochemistry of Cenozoic volcanic rocks of eastern China: implications for their origin from suboceanic-type mantle reservoirs. Earth and Planetary Science Letters 105, 149–169.

Bercovici, D., Karato, S.i., 2003. Whole-mantle convection and the transition-zone water filter. Nature 425, 39–44.

Bijwaard, H., Spakman, W., Engdahl, E.R., 1998. Closing the gap between regional and global travel time tomography. Journal of Geophysical Research 103, 30055–30078.

Campbell, I.H., 2007. Testing the plume theory. Chemical Geology 241, 153–176.

Cao, Q., Wang, P., Van der Hilst, R., De Hoop, M., Shim, S.H., 2010. Imaging the upper mantle transition zone with a generalized radon transform of SS precursors. Physics of the Earth and Planetary Interiors 180, 80–91.

Cao, Q., Van der Hilst, R., De Hoop, M., Shim, S.H., 2011. Seismic imaging of transition zone discontinuities suggests hot mantle west of Hawaii. Science 332, 1068–1071.

Chambers, K., Deuss, A., Woodhouse, J., 2005. Reflectivity of the 410-km discontinuity from PP and SS precursors. Journal of Geophysical Research 110, B02301.

Chen, Y., Zhang, Y., Graham, D., Su, S., Deng, J., 2007. Geochemistry of Cenozoic basalts and mantle xenoliths in Northeast China. Lithos 96, 108–126.

Chen, Y., Gu, Y.J., Dokht, R.M., Sacchi, M.D., 2015. Crustal imprints of Precambrian orogenesis in western Laurentia. Journal of Geophysical Research 120, 6993–7012.

Creager, K.C., Jordan, T.H., 1986. Slab penetration into the lower mantle beneath the Mariana and other island arcs of the northwest Pacific. Journal of Geophysical Research 91, 3573–3589.

Deuss, A., 2009. Global observations of mantle discontinuities using SS and PP precursors. Surveys in Geophysics 30, 301–326.

Dziewonski, A.M., Anderson, D.L., 1981. Preliminary reference earth model. Physics of the Earth and Planetary Interiors 25, 297–356.

Efron, B., Tibshirani, R., 1991. Statistical data analysis in the computer age. Science 253, 390–395.

Faccenna, C., Becker, T.W., Lallemand, S., Lagabrielle, Y., Funiciello, F., Piromallo, C., 2010. Subduction-triggered magmatic pulses: a new class of plumes? Earth and Planetary Science Letters 299, 54–68.

Fei, Y., Bertka, C.M., 1999. Phase Transitions in the Earth's Mantle and Mantle Mineralogy. Mantle Petrology: Field Observations and High Pressure Experimentation Vol. 6 pp. 189–207.

Fichtner, A., Igel, H., 2008. Efficient numerical surface wave propagation through the optimization of discrete crustal models — a technique based on non-linear dispersion curve matching (DCM). Geophysical Journal International 173, 519–533.

Flanagan, M.P., Shearer, P.M., 1998. Global mapping of topography on transition zone velocity discontinuities by stacking SS precursors. Journal of Geophysical Research 103, 2673–2692.

Friederich, W., 1999. Propagation of seismic shear and surface waves in a laterally heterogeneous mantle by multiple forward scattering. Geophysical Journal International 136, 180–204.

Friederich, W., 2003. The S-velocity structure of the East Asian mantle from inversion of shear and surface waveforms. Geophysical Journal International 153, 88–102.

Friederich, W., Dalkolmo, J., 1995. Complete synthetic seismograms for a spherically symmetric earth by a numerical computation of the Green's function in the frequency domain. Geophysical Journal International 122, 537–550.

Frost, D.J., Dolejš, D., 2007. Experimental determination of the effect of H$_2$O on the 410-km seismic discontinuity. Earth and Planetary Science Letters 256, 182–195.

Fukao, Y., Obayashi, M., Inoue, H., Nenbai, M., 1992. Subducting slabs stagnant in the mantle transition zone. Journal of Geophysical Research 97, 4809–4822.

Fukao, Y., Widiyantoro, S., Obayashi, M., 2001. Stagnant slabs in the upper and lower mantle transition region. Reviews of Geophysics 39, 291–323.

Fukao, Y., Obayashi, M., Nakakuki, T., 2009. Stagnant slab: a review. Annual Review of Earth and Planetary Sciences 37, 19–46.

Gorbatov, A., Kennett, B., 2003. Joint bulk-sound and shear tomography for Western Pacific subduction zones. Earth and Planetary Science Letters 210, 527–543.

Gossler, J., Kind, R., 1996. Seismic evidence for very deep roots of continents. Earth and Planetary Science Letters 138, 1–13.

Grand, S.P., 2002. Mantle shear–wave tomography and the fate of subducted slabs. Philosophical Transactions of the Royal Society of London A: Mathematical, Physical and Engineering Sciences 360, 2475–2491.

Grand, S.P., van der Hilst, R.D., Widiyantoro, S., 1997. Global seismic tomography: a snapshot of convection in the earth. GSA Today 7, 1–7.

Gu, Y.J., Dziewonski, A.M., 2002. Global variability of transition zone thickness. Journal of Geophysical Research 107, 2135.

Gu, Y.J., Sacchi, M., 2009. Radon transform methods and their applications in mapping mantle reflectivity structure. Surveys in Geophysics 30, 327–354.

Gu, Y., Dziewonski, A.M., Agee, C.B., 1998. Global de-correlation of the topography of transition zone discontinuities. Earth and Planetary Science Letters 157, 57–67.

Gu, Y.J., Dziewoński, A.M., Ekström, G., 2003. Simultaneous inversion for mantle shear velocity and topography of transition zone discontinuities. Geophysical Journal International 154, 559–583.

Gu, Y.J., Okeler, A., Schultz, R., 2012. Tracking slabs beneath northwestern Pacific subduction zones. Earth and Planetary Science Letters 331, 269–280.

Gudmundsson, Ó., Sambridge, M., 1998. A regionalized upper mantle (RUM) seismic model. Journal of Geophysical Research 103, 7121–7136.

Haupt, R.L., Haupt, S.E., 2004. Practical Genetic Algorithm. Second edition. John Wiley & Sons, New Jersey.

Hayes, G.P., Wald, D.J., Johnson, R.L., 2012. Slab1.0: a three-dimensional model of global subduction zone geometries. Journal of Geophysical Research 117.

Heit, B., Yuan, X., Bianchi, M., Kind, R., Gossler, J., 2010. Study of the lithospheric and upper-mantle discontinuities beneath eastern Asia by SS precursors. Geophysical Journal International 183, 252–266.

Honda, S., Morishige, M., Orihashi, Y., 2007. Sinking hot anomaly trapped at the 410 km discontinuity near the Honshu subduction zone, Japan. Earth and Planetary Science Letters 261, 565–577.

Houser, C., Williams, Q., 2010. Reconciling Pacific 410 and 660 km discontinuity topography, transition zone shear velocity patterns, and mantle phase transitions. Earth and Planetary Science Letters 296, 255–266.

Huang, J., Zhao, D., 2006. High-resolution mantle tomography of China and surrounding regions. Journal of Geophysical Research 111, B09305.

Ichiki, M., Baba, K., Obayashi, M., Utada, H., 2006. Water content and geotherm in the upper mantle above the stagnant slab: interpretation of electrical conductivity and seismic P-wave velocity models. Physics of the Earth and Planetary Interiors 155, 1–15.

Ito, E., Takahashi, E., 1989. Postspinel transformations in the system Mg$_2$SiO$_4$-Fe$_2$SiO$_4$ and some geophysical implications. Journal of Geophysical Research 94, 10637–10646.

Jackson, M.G., Dasgupta, R., 2008. Compositions of HIMU, EM1, and EM2 from global trends between radiogenic isotopes and major elements in ocean island basalts. Earth and Planetary Science Letters 276, 175–186.

Jordan, T., 1977. Lithospheric slab penetration into the lower mantle beneath the Sea of Okhotsk. Journal of Geophysics 43, 473–496.

Katsura, T., Ito, E., 1989. The system Mg_2SiO_4-Fe_2SiO_4 at high pressures and temperatures: precise determination of stabilities of olivine, modified spinel, and spinel. Journal of Geophysical Research 94, 15663–15670.

Kuritani, T., Kimura, J.I., Miyamoto, T., Wei, H., Shimano, T., Maeno, F., Jin, X., Taniguchi, H., 2009. Intraplate magmatism related to deceleration of upwelling asthenospheric mantle: implications from the Changbaishan shield basalts, northeast China. Lithos 112, 247–258.

Larson, R., 1991. Latest pulse of earth: evidence for a mid-cretaceous superplume. Geology 19, 547–550.

Laske, G., Masters, G., Ma, Z., Pasyanos, M., 2013. Update on CRUST1.0 - A 1-Degree Global Model of Earth's Crust 15, Abstract EGU2013–2658.

Lawrence, J.F., Shearer, P.M., 2006a. Constraining seismic velocity and density for the mantle transition zone with reflected and transmitted waveforms. Geochemistry, Geophysics, Geosystems 7.

Lawrence, J.F., Shearer, P.M., 2006b. A global study of transition zone thickness using receiver functions. Journal of Geophysical Research 111, B06307.

Lebedev, S., Nolet, G., 2003. Upper mantle beneath Southeast Asia from S velocity tomography. Journal of Geophysical Research - Solid Earth 108.

Lebedev, S., van der Hilst, R.D., 2008. Global upper-mantle tomography with the automated multimode inversion of surface and S-wave forms. Geophysical Journal International 173, 505–518.

Lei, J., Zhao, D., 2005. P-wave tomography and origin of the Changbai intraplate volcano in Northeast Asia. Tectonophysics 397, 281–295.

Lessing, S., Thomas, C., Rost, S., Cobden, L., Dobson, D.P., 2014. Mantle transition zone structure beneath India and Western China from migration of PP and SS precursors. Geophysical Journal International 197, 396–413.

Lessing, S., Thomas, C., Saki, M., Schmerr, N., Vanacore, E., 2015. On the difficulties of detecting PP precursors. Geophysical Journal International 201, 1666–1681.

Li, C., van der Hilst, R.D., 2010. Structure of the upper mantle and transition zone beneath Southeast Asia from traveltime tomography. Journal of Geophysical Research 115.

Li, X., Yuan, X., 2003. Receiver functions in northeast China — implications for slab penetration into the lower mantle in northwest Pacific subduction zone. Earth and Planetary Science Letters 216, 679–691.

Li, X., Sobolev, S., Kind, R., Yuan, X., Estabrook, C., 2000. A detailed receiver function image of the upper mantle discontinuities in the Japan subduction zone. Earth and Planetary Science Letters 183, 527–541.

Li, X., Kind, R., Yuan, X., 2003. Seismic study of upper mantle and transition zone beneath hotspots. Physics of the Earth and Planetary Interiors 136, 79–92.

Li, C., van der Hilst, R.D., Engdahl, E.R., Burdick, S., 2008. A new global model for P wave speed variations in Earth's mantle. Geochemistry, Geophysics, Geosystems 9.

Liu, Q., Gu, Y., 2012. Seismic imaging: from classical to adjoint tomography. Tectonophysics 566, 31–66.

Liu, Z., Niu, F., Chen, Y.J., Grand, S., Kawakatsu, H., Ning, J., Tanaka, S., Obayashi, M., Ni, J., 2015. Receiver function images of the mantle transition zone beneath ne China: new constraints on intraplate volcanism, deep subduction and their potential link. Earth and Planetary Science Letters 412, 101–111.

Marone, F., Gung, Y., Romanowicz, B., 2007. Three-dimensional radial anisotropic structure of the North American upper mantle from inversion of surface waveform data. Geophysical Journal International 171, 206–222.

Mégnin, C., Romanowicz, B., 2000. The three-dimensional shear velocity structure of the mantle from the inversion of body, surface and higher-mode waveforms. Geophysical Journal International 143, 709–728.

Navrotsky, A., 1980. Lower mantle phase transitions may generally have negative pressure–temperature slopes. Geophysical Research Letters 7, 709–711.

Niu, Y., 2005. Generation and evolution of basaltic magmas: some basic concepts and a new view on the origin of Mesozoic–Cenozoic basaltic volcanism in eastern China. Geological Journal of China Universities 11, 9–46.

Obayashi, M., Sugioka, H., Yoshimitsu, J., Fukao, Y., 2006. High temperature anomalies oceanward of subducting slabs at the 410-km discontinuity. Earth and Planetary Science Letters 243, 149–158.

Ohtani, E., Litasov, K., Hosoya, T., Kubo, T., Kondo, T., 2004. Water transport into the deep mantle and formation of a hydrous transition zone. Physics of the Earth and Planetary Interiors 143, 255–269.

Priestley, K., Debayle, E., McKenzie, D., Pilidou, S., 2006. Upper mantle structure of eastern Asia from multimode surface waveform tomography. Journal of Geophysical Research - Solid Earth 111 (B10).

Revenaugh, J., Jordan, T.H., 1991. Mantle layering from ScS reverberations: 2. The transition zone. Journal of Geophysical Research 96, 19763–19780.

Ritsema, J., Deuss, A., Van Heijst, H., Woodhouse, J., 2011. S40RTS: a degree-40 shear-velocity model for the mantle from new Rayleigh wave dispersion, teleseismic traveltime and normal-mode splitting function measurements. Geophysical Journal International 184, 1223–1236.

Rost, S., Thomas, C., 2009. Improving seismic resolution through array processing techniques. Surveys in Geophysics 30, 271–299.

Sacchi, M.D., 1998. A bootstrap procedure for high-resolution velocity analysis. Geophysics 63, 1716–1725.

Schmandt, B., Humphreys, E., 2010. Complex subduction and small-scale convection revealed by body-wave tomography of the western United States upper mantle. Earth and Planetary Science Letters 297, 435–445.

Schmerr, N., Garnero, E., 2006. Investigation of upper mantle discontinuity structure beneath the central Pacific using SS precursors. Journal of Geophysical Research 111, B08305.

Schmerr, N., Garnero, E.J., 2007. Upper mantle discontinuity topography from thermal and chemical heterogeneity. Science 318, 623–626.

Schmerr, N., Thomas, C., 2011. Subducted lithosphere beneath the Kuriles from migration of PP precursors. Earth and Planetary Science Letters 311, 101–111.

Shearer, P.M., 1991. Constraints on upper mantle discontinuities from observations of long-period reflected and converted phases. Journal of Geophysical Research 96, 18147–18182.

Shearer, P.M., 1993. Global mapping of upper mantle reflectors from long-period SS precursors. Geophysical Journal International 115, 878–904.

Shearer, P.M., Flanagan, M.P., Hedlin, M.A., 1999. Experiments in migration processing of ss precursor data to image upper mantle discontinuity structure. Journal of Geophysical Research - Solid Earth 104, 7229–7242.

Simmons, N.A., Forte, A.M., Boschi, L., Grand, S.P., 2010. Gypsum: a joint tomographic model of mantle density and seismic wave speeds. Journal of Geophysical Research - Solid Earth 115.

Stoffa, P.L., Sen, M.K., 1991. Nonlinear multiparameter optimization using genetic algorithms: inversion of plane-wave seismograms. Geophysics 56, 1794–1810.

Tang, Y., Obayashi, M., Niu, F., Grand, S.P., Chen, Y.J., Kawakatsu, H., Tanaka, S., Ning, J., Ni, J.F., 2014. Changbaishan volcanism in northeast China linked to subduction-induced mantle upwelling. Nature Geoscience 7, 470–475.

Tatsumi, Y., Maruyama, S., Nohda, S., 1990. Mechanism of backarc opening in the Japan Sea: role of asthenospheric injection. Tectonophysics 181, 299–306.

Tatsumi, Y., Shinjoe, H., Ishizuka, H., Sager, W.W., Klaus, A., 1998. Geochemical evidence for a mid-Cretaceous superplume. Geology 26, 151–154.

Tauzin, B., Debayle, E., Wittlinger, G., 2008. The mantle transition zone as seen by global Pds phases: no clear evidence for a thin transition zone beneath hotspots. Journal of Geophysical Research - Solid Earth 113, B08309.

van der Hilst, R., Engdahl, E., Spakman, W., Nolet, G., 1991. Tomographic imaging of subducted lithosphere below northwest Pacific island arcs. Nature 353, 37–42.

van der Hilst, R., Engdahl, E., Spakman, W., 1993. Tomographic inversion of P and pP data for aspherical mantle structure below the northwest Pacific region. Geophysical Journal International 115, 264–302.

Weidner, D.J., Wang, Y., 1998. Chemical-and Clapeyron-induced buoyancy at the 660 km discontinuity. Journal of Geophysical Research 103, 7431–7441.

Ye, L., Li, J., Tseng, T.L., Yao, Z., 2011. A stagnant slab in a water-bearing mantle transition zone beneath northeast China: implications from regional SH waveform modelling. Geophysical Journal International 186, 706–710.

Yuan, H., Romanowicz, B., 2010. Lithospheric layering in the North American craton. Nature 466, 1063–1068.

Zhao, D., 2007. Seismic images under 60 hotspots: search for mantle plumes. Gondwana Research 12, 335–355.

Zhao, D., Liu, L., 2010. Deep structure and origin of active volcanoes in China. Geoscience Frontiers 1, 31–44.

Zhao, D., Ohtani, E., 2009. Deep slab subduction and dehydration and their geodynamic consequences: evidence from seismology and mineral physics. Gondwana Research 16, 401–413.

Zhao, D., Lei, J., Tang, R., 2004. Origin of the Changbai intraplate volcanism in Northeast China: evidence from seismic tomography. Chinese Science Bulletin 49, 1401–1408.

Zhao, D., Yanada, T., Hasegawa, A., Umino, N., Wei, W., 2012. Imaging the subducting slabs and mantle upwelling under the Japan Islands. Geophysical Journal International 190, 816–828.

Zheng, Z., Romanowicz, B., 2012. Do double SS precursors mean double discontinuities? Geophysical Journal International 191, 1361–1373.